Molecular engineering of polymeric carbon nitride for highly efficient photocatalytic oxytetracycline degradation and H_2O_2 production

Yang Yang, Guangming Zeng*, Danlian Huang*, Chen Zhang*, Donghui He, Chengyun Zhou, Wenjun Wang, Weiping Xiong, Xiaopei Li, Bisheng Li, Wanyue Dong, Yin Zhou

College of Environmental Science and Engineering, Hunan University and Key Laboratory of Environmental Biology and Pollution Control (Hunan University), Ministry of Education, Changsha 410082, PR China

* Corresponding authors at: College of Environmental Science and Engineering, Hunan University, Changsha, 410082, PR China.

E-mail addresses: zgming@hnu.edu.cn (G. Zeng), huangdanlian@hnu.edu.cn (D. Huang) and zhangchen@hnu.edu.cn (C. Zhang).

Abstract

Developing highly efficient photocatalysts for refractory pollutants degradation and hydrogen peroxide (H_2O_2) production is an ideal strategy to tackle environmental pollution and energy crisis. Herein, we synthesize a novel 2-hydroxy-4,6-dimethylpyrimidine (HDMP) grafted polymeric carbon nitride (CN) photocatalyst (ACN) by a facile in situ keto-enol cyclization method for addressing these issues. The photogenerated electrons and holes are migrated to HDMP and heptazine moiety, respectively. And the average decay lifetime of photogenerated charges of CN and ACN-10 is increased form (222 ±23) to (289 ±38) ps. Benefiting from the controllable electronic migration and accelerated intramolecular charge separation, the ACN photocatalyst exhibits a superior visible-light-driven photocatalytic activity for oxytetracycline degradation and H_2O_2 production. This work makes an insight into the intramolecular charge dynamics in CN, and presents a promising approach to the oxytetracycline degradation and H_2O_2 production.

Keywords: carbon nitride; molecular engineering; photocatalysis; oxytetracycline degradation; H_2O_2 production

1. Introduction

With the rapid growth of industrialization and urbanization in recent years, the environmental pollution and energy crisis have been considered as two major challenges across the world [1-5]. Oxytetracycline (OTC) is a widely used prophylactic antibiotic with the merits of broad-spectrum activity and low cost. But the exposed OTC in water bodies will adversely affect ecological systems via restraining the growth of microorganisms, inducing the generation of antibiotic resistant bacteria and bringing about other ecotoxicological effects [6-9]. Meanwhile, as an ideal alternative energy carrier to H_2 in fuel cell, hydrogen peroxide (H_2O_2) has attracted much interest owing to its convenience and safety in store and transport, and the capability to be utilized in single-compartment direct peroxide-peroxide fuel cell (DPPFC) [10, 11]. In addition, H_2O_2 is also a clean and versatile oxidant, which has been efficiently applied to the pulp bleaching, disinfection and environmental remediation [12-14]. Nevertheless, traditional technologies such as anthraquinone method and electrocatalytic oxygen reduction reaction (ORR) route often present complicated processes, high risks, potential pollutions and high costs, which greatly restrict their large-scale practical application [15-17].

As a desirable technology to address these problems, semiconductor photocatalysis which can directly utilize solar energy to activate molecular oxygen to generate reactive oxygen species (ROS) is a promising way for the degradation of refractory pollutants and synthesis of H_2O_2 [18-22]. Among the numerous explored photocatalysts, polymeric carbon nitride (CN) has emerged as the ideal candidate due to its favorable band gap, chemical stability, abundance and environmental benignity [23-26]. Since the pioneering work reported in 2009 by Wang et al. [27], CN has been frequently employed in the field of photocatalysis, such as photocatalytic H_2 evolution, photocatalytic CO_2 reduction and photocatalytic organic pollutants degradation. In particular, Shiraishi et al. [28] found

that CN presented a high selectivity for H_2O_2 production under visible light irradiation ($\lambda > 420$ nm) in water with alcohol and O_2 owing to the efficient formation of 1,4-endoperoxide on its surface. However, pristine CN generally suffers from insufficient visible light absorption, low conductivity, and high recombination rate of photogenerated charge carriers, resulting in very poor photocatalytic performance [29-32].

Recently, the strategy of molecular engineering was executed in CN to greatly improve the photocatalytic performance by modulating the band structure and the electronic structure for the extended optical absorption and the accelerated charge transfer [33]. For example, our group achieved superior photocatalytic degradation of sulfamethazine under visible light irradiation, by incorporating 2,5-dibromopyrazine into CN networks through a bottom-up method, to enhance visible light absorption and boost charge carrier separation [34]. Kofuji et al. [35] successfully incorporated biphenyl diimide into the CN framework, with photocatalytic performance for H_2O_2 production remarkably enhanced as compared to pristine CN, owing to the electron-deficient biphenyl diimide giving rise to the accelerated separation of photogenerated charge carriers. Kim et al. [36] demonstrated that anthraquinone could endow CN with abundant H_2O_2 evolution site, extended spectral absorption, and improved separation and transfer of photogenerated charge carriers, contributing to the significantly enhanced photocatalytic activity for H_2O_2 production. These previous studies indicate that molecular engineering could highly efficient elevate the photocatalytic activity of CN. Nevertheless, the investigation of molecular engineering on CN is still at an early stage, and most reported samples have been developed in a complex process. More importantly, the precise control of local electronic migration and the understanding of charge separation in molecular level is still insufficient. In this regard, it is necessary to develop a facile route to precisely modulate the structure of CN, and deeply explore the fundamental mechanism of charge carrier dynamics.

In this work, we develop a facile approach to control the electronic structure of CN by an in situ keto-enol cyclization route of urea and acetylacetone, incorporating the 2-hydroxy-4,6-dimethylpyrimidine (HDMP) into the molecular framework of CN. The morphologies and structures, optical and photoelectrochemical properties of the obtained samples are detailedly characterized and compared. Subsequently, their electronic structures are elucidated by the density functional theory (DFT) calculations. More importantly, the separation dynamics of photogenerated charges are investigated by photoluminescence (PL) spectra, time-resolved photoluminescence (TRPL) spectra and femtosecond transient absorption (fs-TA) spectra. Finally, their photocatalytic performances and mechanisms for the OTC degradation and H_2O_2 production are evaluated under visible light irradiation.

2. Experimental Section

2.1. Synthesis of CN and ACN

All the raw materials were of analytical grade and used without further purification. In a typical synthesis procedure, a certain volume of acetylacetone and 10 g of urea were mixed. Then the resulting mixture was placed in a covered alumina crucible and heated to 550 ℃ for 3 h with a ramp rate of 3 ℃ min^{-1}. After cooled to room temperature, the product was washed with deionized water several times and dried at 70 ℃ for 12 h. The samples were denoted as ACN-5, ACN-10 and ACN-30, with the volumes of acetylacetone in the initial precursor being 5, 10 and 30 μL, respectively. For comparison, the pristine CN was synthesized without adding acetylacetone. Besides, the volume of acetylacetone was increased to 200 μL (denoted as ACN-200) for the analysis of solid-state ^{13}C nuclear magnetic resonance (NMR).

2.2. Characterization

Scanning electron microscopy (SEM) images were collected using a Zeiss Gemini 300 electron

microscope. Transmission electron microscopy (TEM) images were acquired on a FEI Tecnai G2 F20 S-TWIN electron microscope. Nitrogen adsorption-desorption isotherms were recorded on a Micromeritics ASAP 2020 HD88 instrument. X-ray diffraction (XRD) patterns were performed on a Bruker D8 Focus diffractometer using a Cu Kα radiation source. Raman measurements were conducted on a Horiba Jobin Yvon LabRAM HR800 Raman spectrometer with an excitation wavelength of 325 nm. Attenuated total reflectance Fourier-transform infrared (ATR-FTIR) spectra were obtained using a Thermo Nicolet 5700 spectrophotometer. Solid-state ^{13}C NMR spectra were measured on a Bruker Avance III 600 spectrometer with cross-polarization magic angle spinning. X-ray photoelectron spectroscopy (XPS) spectra were acquired using a Thermo Escalab 250Xi spectrometer with Al Kα as the excitation source. UV-vis diffuse reflectance spectra (DRS) were obtained on a PerkinElmer Lambda 750 UV/vis/NIR spectrophotometer. Electron spin resonance (ESR) spectra were recorded on a JEOL model JES-FA200 ESR spectrometer. PL spectra were collected using a PerkinElmer LS-55 fluorescence spectrophotometer. TRPL spectra were recorded on a FLS 980 fluorescence lifetime spectrophotometer. fs-TA measurements were performed on a Helios pump-probe system (Ultrafast Systems LLC) combined with an amplified femtosecond laser system (Coherent).

2.3. Theoretical computation

Gaussian program was employed for DFT calculations. Geometry optimization was performed at M06-2X/def2-SVP level. Wavefunction analysis was carried out with Multiwfn program. Due to the fact that M06-2X tends to overestimate highest occupied molecular orbital (HOMO)-lowest unoccupied molecular orbital (LUMO) gap, although it usually gives better geometry and density, the HOMO and LUMO energies were calculated with the B3LYP functional.

2.4. Photoelectrochemical test

The photoelectrochemical tests were performed on a Chenhua CHI 760E electrochemical workstation with a standard three-electrode cell in 0.2 mol L^{-1} Na_2SO_4 electrolyte using Ag/AgCl electrode, Pt wire electrode and sample electrode as the reference electrode, counter electrode and working electrode, respectively. The working electrode was fabricated as follows: 5 mg of the sample was uniformly dispersed in 1 mL of 10% nafion solution to produce a slurry. Then, the slurry was coated onto a fluorine-doped tinoxide (FTO) glass (effective area: 1 cm^2) and dried at 80 ℃ for 4 h. For transient photocurrent test, a 300 W xenon lamp (PLS-SXE300/300UV, Perfect Light) equipped with a 420 nm cutoff filter was utilized to provide light source. Electrochemical impedance spectroscopy (EIS) were recorded in the frequency range of 10^{-2} to 10^5 Hz. Mott-Schottky plots were collected at different frequencies of 0.5, 1 and 1.5 kHz.

Rotating disk electrode (RDE) measurements were performed on a Chenhua CHI 760E electrochemical workstation with a standard three-electrode cell using Ag/AgCl electrode, Pt wire electrode and sample electrode as the reference electrode, counter electrode and working electrode, respectively. The working electrode was prepared as follows: 5 mg of the sample was homogeneously dispersed in 0.5 mL of 10% nafion solution (diluted with ethanol) to form a slurry. Then, 5 μL of the slurry was dropped on a glassy carbon electrode (diameter of 5 mm) and dried at room temperature. The linear sweep voltammetry (LSV) curves were collected with a scan rate of 10 mV s^{-1} in an O_2-saturated phosphate buffer solution (pH 7).

2.5. Photocatalytic OTC degradation

During each photocatalytic test, 30 mg of the sample was dispersed into an aqueous solution of OTC hydrochloride (100 mL, 20 mg L^{-1}). Prior to irradiation, the suspension was stirred in the dark for 30 min to achieve the adsorption-desorption equilibrium. A 300 W xenon lamp (PLS-SXE300/300UV, Perfect Light) equipped with a 420 nm cutoff filter was employed as the light source.

During irradiation, 3 mL of the suspension was taken out at a 15 min interval, and centrifuged and filtrated (0.45 μm Millipore filter) to remove the powder before measurement. The peak absorbance of OTC at 353 nm was used to determine its concentration by a Shimadzu UV-2700 spectrophotometer. A liquid chromatography coupled with tandem mass spectrometry (LC-MS/MS) system was utilized to identify the degradation intermediates of OTC. A Shimadzu TOC-VCPH analyzer was employed to analyze the total organic carbon (TOC). To evaluate the stability of the photocatalyst, the sample was collected through centrifugation after one trial, and washed with deionized water and ethanol, and then dried for the cycle experiment. In trapping experiments, reactive species generated by the ACN-10 were quenched by adding 5 mmol L^{-1} of 4-hydroxy-2,2,6,6-tetramethylpiperidinyloxy (TEMPOL, $\bullet O_2^-$ quencher), 5 mmol L^{-1} of isopropanol (IPA, •OH quencher) and 5 mmol L^{-1} of ethylenediaminetetraacetic acid disodium (EDTA-2Na, h^+ quencher).

2.6. Photocatalytic H_2O_2 production

During each photocatalytic experiment, 50 mg of the sample was added into 50 mL of aqueous solution containing 10 vol% IPA. Before irradiation, the suspensions were ultrasonically dispersed for 5 min in the dark, and then stirred for 60 min with O_2 bubbling to ensure the adsorption-desorption equilibrium. The light source was provided by a 300 W xenon lamp (PLS-SXE300/300UV, Perfect Light) equipped with a 420 nm cutoff filter. At specific time intervals, 3 mL of the suspension was gathered, centrifuged and filtrated (0.45 μm Millipore filter) for analyzing the concentration of H_2O_2 (iodometry) [37]. The cycle experiments were conducted to evaluate the stability of the sample.

3. Results and Discussion

3.1. Morphology and structure

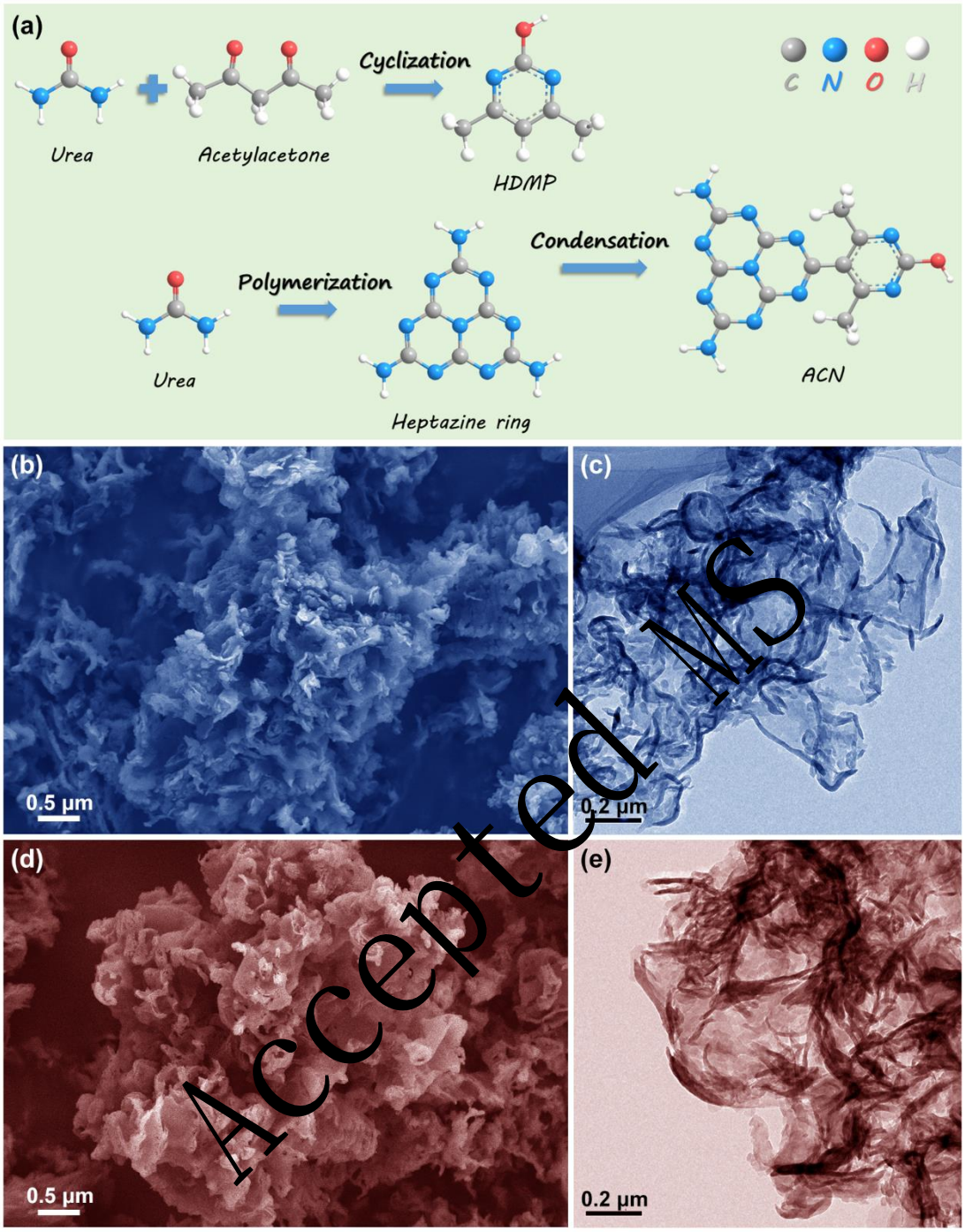

Fig. 1. (a) The synthetic process of incorporating HDMP into the CN frameworks; SEM and TEM images of the (b and c) CN and (d and e) ACN-10.

The schematic diagram for the formation mechanism of ACN sample is displayed in Fig. 1a. As depicted, the urea and acetylacetone undergo in situ keto-enol cyclization to form the HDMP. And meanwhile, the heptazine ring is generated via the polymerization of urea. Then the ACN sample is formed by the bimolecular condensation between the HDMP and heptazine ring. The morphologies

of the CN and ACN-10 samples are observed by SEM and TEM. As displayed in Fig. 1b and c, CN exhibits typical sheet-like structures with coarse surfaces. Compared with CN, the morphology of ACN-10 (Fig. 1d and e) is not changed significantly due to the less addition of acetylacetone. Moreover, the specific surface areas and pores of the samples are investigated by nitrogen adsorption-desorption isotherms. As shown in Fig. S1, both CN and ACN samples hold type IV isotherm and similar mesopore distribution. The Brunauer-Emmett-Teller (BET) specific surface area and pore volume of ACN-10 is 67.81 $m^2 g^{-1}$ and 0.33 $cm^3 g^{-1}$, respectively, which are smaller than those of CN (77.40 $m^2 g^{-1}$ and 0.41 $cm^3 g^{-1}$, respectively), indicating that the specific surface area is not the dominant factor affecting the photocatalytic activity.

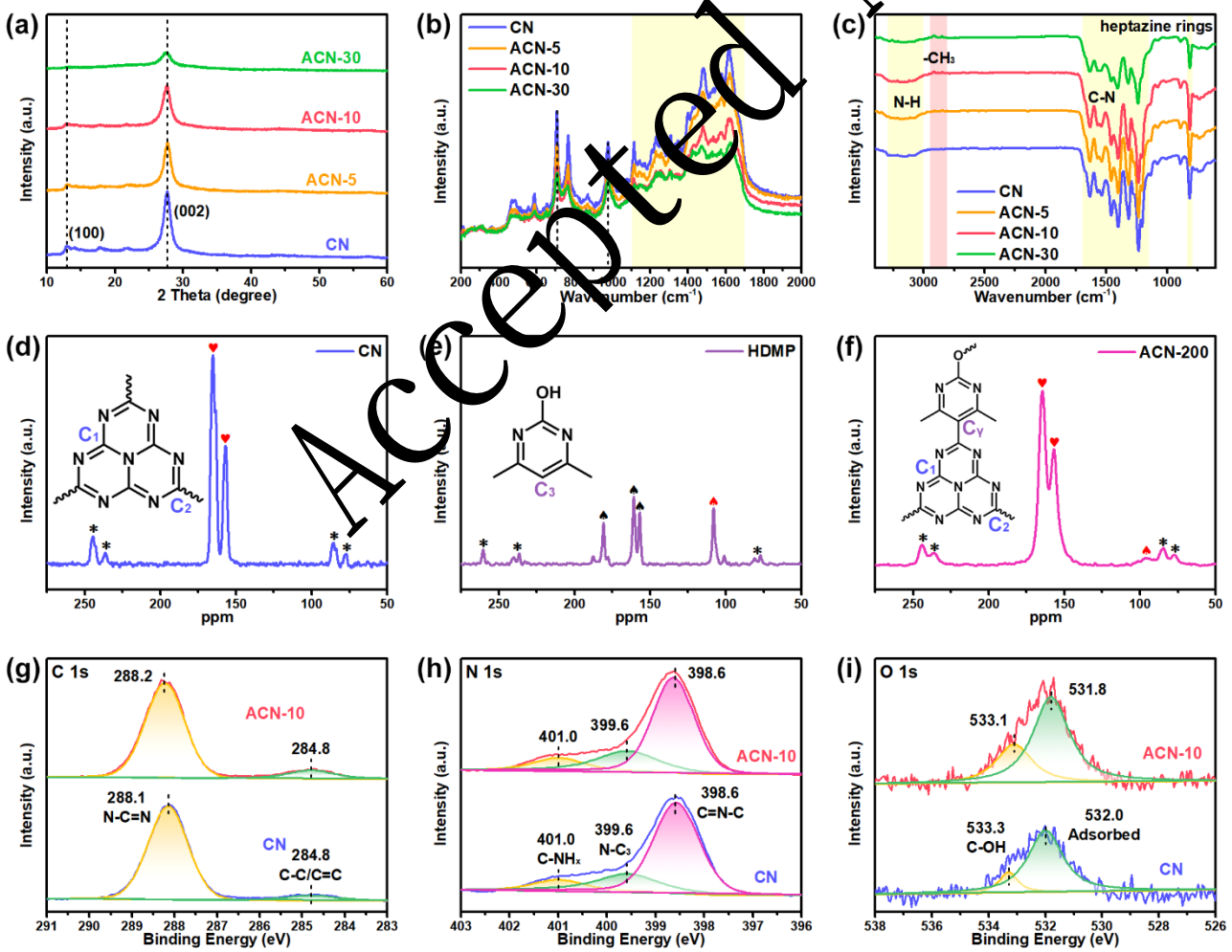

Fig. 2. (a) XRD patterns, (b) Raman spectra and (c) ATR-FTIR spectra of the samples; Solid-state ^{13}C NMR

spectra of the (d) CN, (e) HDMP and (f) ACN-200 (the symbols of *, ♥ and ♠ indicate the spinning sidebands of solid-state ^{13}C NMR spectra, the characteristic peaks of CN and the characteristic peaks of HDMP, respectively); (g) C 1s, (h) N 1s and (i) O 1s XPS spectra of the CN and ACN-10.

The structures of the samples are then analyzed by XRD patterns, Raman spectra and ATR-FTIR spectra. In the XRD patterns of CN and ACN samples (Fig. 2a), two peaks at 12.9 ° and 27.7 ° are ascribed to the in-plane repeating heptazine units and stacking of conjugated aromatic planes, which can be assigned to the (100) and (002) planes, respectively [38]. Compared with CN, these peaks of ACN samples become broader and weaker, implying that the planar structure of CN is distorted by HDMP to varying degrees. Raman spectra of CN and ACN samples in Fig. 2b display the similar characteristic peaks at 707, 977 and 1100-1700 cm^{-1}, which can be indexed to the in-plane bending, the symmetric N-breathing mode of heptazine and the disordered graphitic C-N vibrations, respectively [39]. In comparison with CN, the Raman peaks of ACN samples are much weaker, which are attributed to the more disordered structure induced by the graft of HDMP. Additionally, ATR-FTIR spectra of the samples are shown in Fig. 2c. Obviously, ACN samples possess similar but broadened and less sharp peaks comparing to CN because of the implantation of HDMP into the pristine CN structure. The peaks in the 810, 1150-1700 and 3000-3300 cm^{-1} regions represent the heptazine rings, aromatic C-N heterocycles and vibrational absorption of N-H group, respectively [40]. As the amount of acetylacetone increases, peaks of all ACN samples at 2810-2950 cm^{-1} related to the stretching vibration of $-CH_3$ are gradually getting stronger than those of CN (Fig. S2) [41], demonstrating the existence of HDMP in the ACN frameworks.

To further prove the successful incorporation of HDMP into the CN networks, solid-state ^{13}C NMR test is carried out. As displayed in solid-state ^{13}C NMR spectrum of CN (Fig. 2d), the CN presents two carbon peaks at 157 and 165 ppm, which are attributed to C_1 (CN_3) and C_2 ($CN_2(NH_x)$)

carbons, respectively [42]. Four distinct carbon peaks at 108, 157, 161 and 181 ppm can be observed in HDMP, as shown in Fig. 2e. Due to the formation of self-assembled structures between pyrimidine derivatives, the only peak that can be identified is located at 108 ppm, corresponding to C_3 (CC_2) carbon [43]. However, in comparison with CN, the ACN-10 exhibits no obvious changes on the solid-state ^{13}C NMR spectrum (Fig. S3). In order to observe the changes of solid-state ^{13}C NMR spectrum more clearly, the control sample (ACN-200) with 20 times higher volume with respect to the acetylacetone used to prepare ACN-10 is synthesized. As exhibited in Fig. 2f, the ACN-200 presents a new peak at 96 ppm, which can be attributed to the Cγ (CC_3) carbon *para* to the hydroxyl group of HDMP. Compared to HDMP, this peak is downshifted, indicating that this carbon is in a more electron-rich chemical environment. Meanwhile, ACN-200 shows decrease in the intensity of C_2 ($CN_2(NH_x)$) carbon because of the graft of HDMP. These results of solid-state ^{13}C NMR spectra demonstrate that the HDMP moiety is successfully incorporated into the CN frameworks, and the heptazine unit and HDMP are connected via the Cγ carbon.

The surface chemical compositions and states of the CN and ACN-10 are then investigated by XPS. As shown in the survey spectra (Fig. S4), C, N and O elements exist in all of the samples. In C 1s spectra (Fig. 2g), both CN and ACN-10 exhibit peaks at 284.8 and 288.1 eV, corresponding to the graphitic carbon (C-C/C=C) and sp^2-hybridized carbon (N-C=N), respectively [44]. The relatively stronger peak intensity of C-C/C=C for ACN-10 is owing to the existence of aromatic rings in HDMP. The N 1s spectra of CN and ACN-10 possess three similar characteristic peaks (Fig. 2h). The three peaks at 398.6, 399.6 and 401.0 eV can be ascribed to the sp^2-hybridized nitrogen (C=N-C), tertiary nitrogen (N-C_3) and terminal amino groups (C-NH_x), respectively [45]. For O 1s spectra (Fig. 2i), two peaks at 532.0 and 533.3 eV are assigned to the adsorbed H_2O and C-OH bond [46]. An obvious increase in the C-OH intensity is found for ACN-10 in comparison with that of CN because of the

presence of C-OH bond in HDMP. Moreover, the elemental composition (atom ratios) of CN and ACN-10 obtained from XPS are listed in Table S1. A gradual increase in the C/N atom ratio from 0.748 for CN to 0.773 for ACN-10 further reveals the successful integration of the HDMP moiety into the CN frameworks.

3.2. Optical and photoelectrochemical properties

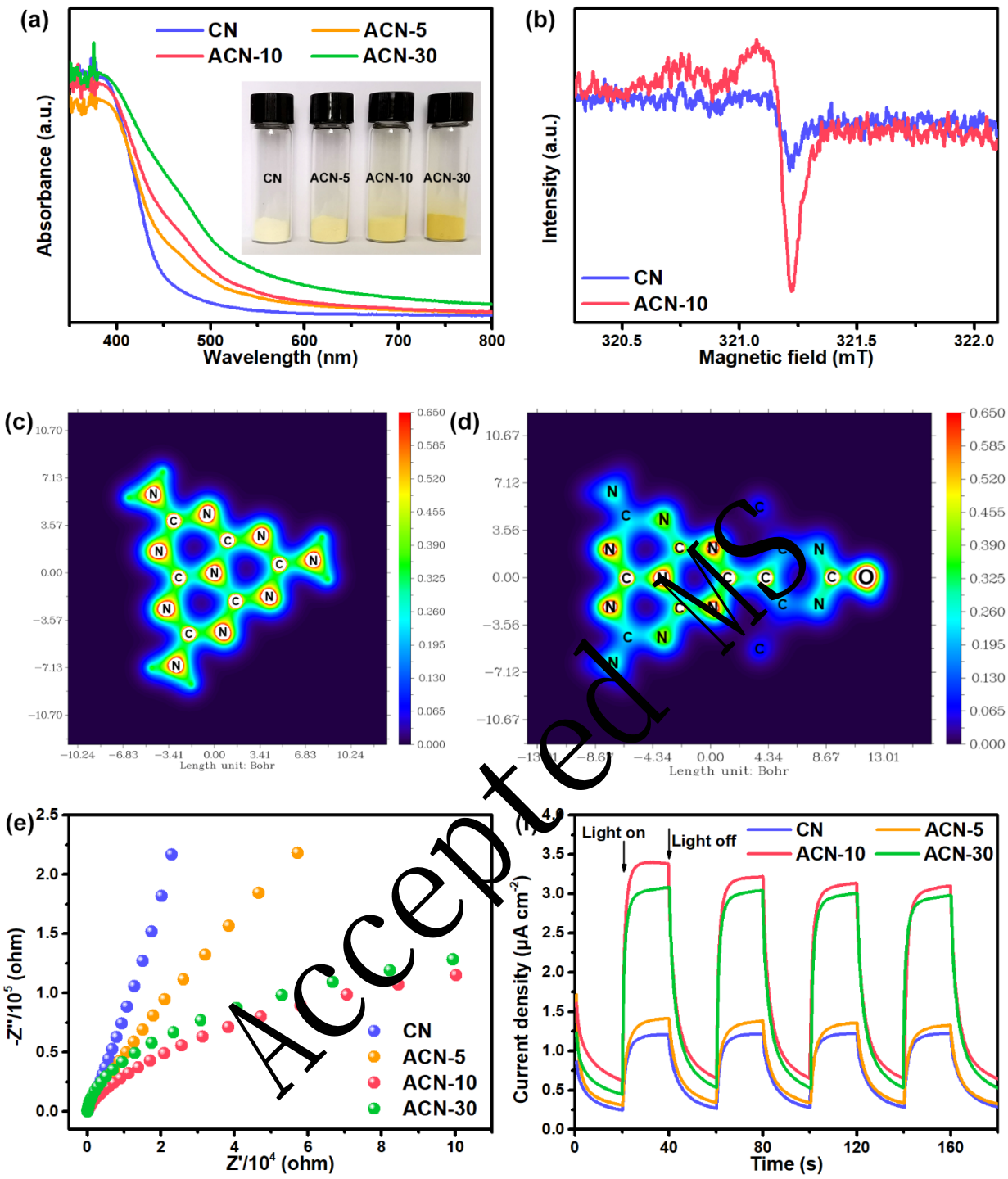

Fig. 3. (a) UV-vis DRS spectra and a photograph (inset), and (b) ESR spectra of the samples; Two-dimensional valence-electron density color-filled maps of the (c) CN and (d) ACN; (e) EIS Nyquist plots and (f) transient photocurrent response curves of the samples.

Generally, the light harvesting ability of the photocatalyst and corresponding separation, transfer and recombination behaviors of photogenerated charges play decisive roles in photocatalytic activity.

The optical absorption properties of the samples are investigated by UV-vis DRS. As displayed in Fig. 3a, CN possesses an optical absorption edge of 450 nm, while ACN-10 exhibits an extended absorption edge of nearly 560 nm. Compared to CN, ACN samples show an enhanced visible light absorption, which is ascribed to an increase of the delocalized π-electrons because the incorporation of HDMP [47]. Moreover, the colors of the samples are in accordance with the results of UV-vis DRS analysis as shown in the insert image of Fig. 3a. To analyze the electronic band structure, ESR spectra of the samples are recorded and the results are displayed in Fig. 3b. Both CN and CAN-10 samples present a paramagnetic absorption signal with the g value of 2.0032, deriving from the unpaired electrons on sp^2-hybridized carbon atoms within the π-conjugated aromatic rings [48]. The intensity of ESR signal of the ACN-10 is higher than that of the CN, indicating more electron delocalization in π-conjugated system after the incorporation of HDMP, which will be in favor of separation and transfer of photogenerated charges during photocatalytic reaction.

To intuitively investigate the subtle alterations of electronic migration, theoretical calculations of electron density are conducted. As displayed in Fig. 3c and d, the state of electronic configuration for the CN and ACN are revealed by the two-dimensional valence-electron density color-filled maps. Compared to CN, the electronic configuration of ACN exhibits an obvious change. In ACN, the O atom presents the highest density, demonstrating the strongest electron-withdrawing ability. Meanwhile, the charge of C atoms and N atoms in ACN are clearly different from that in CN, which may be due to the uneven charge distribution induced by the electronic migration [49]. Therefore, it is suggested that the presence of HDMP will afford a driving force to promote the transfer of electrons through uncoordinated polarity [50].

The photoelectrochemical properties of the samples are evaluated by the EIS and transient photocurrent response. As displayed in Fig. 3e, EIS are collected to investigate their electronic

conductivity. Obviously, ACN-10 possesses the decreased semicircle diameter in comparison with CN, implying that the ACN-10 has a lower electron transfer resistance, which is beneficial for obtaining efficient charge separation and transfer during the photocatalysis [51]. Additionally, Fig. 3f exhibits the transient photocurrent responses of the samples under visible light on or off. After the incorporation of HDMP into CN, ACN-10 appears approximately three times higher photocurrent density than that of CN, indicating the photogenerated charges separate and transfer more efficiently [52].

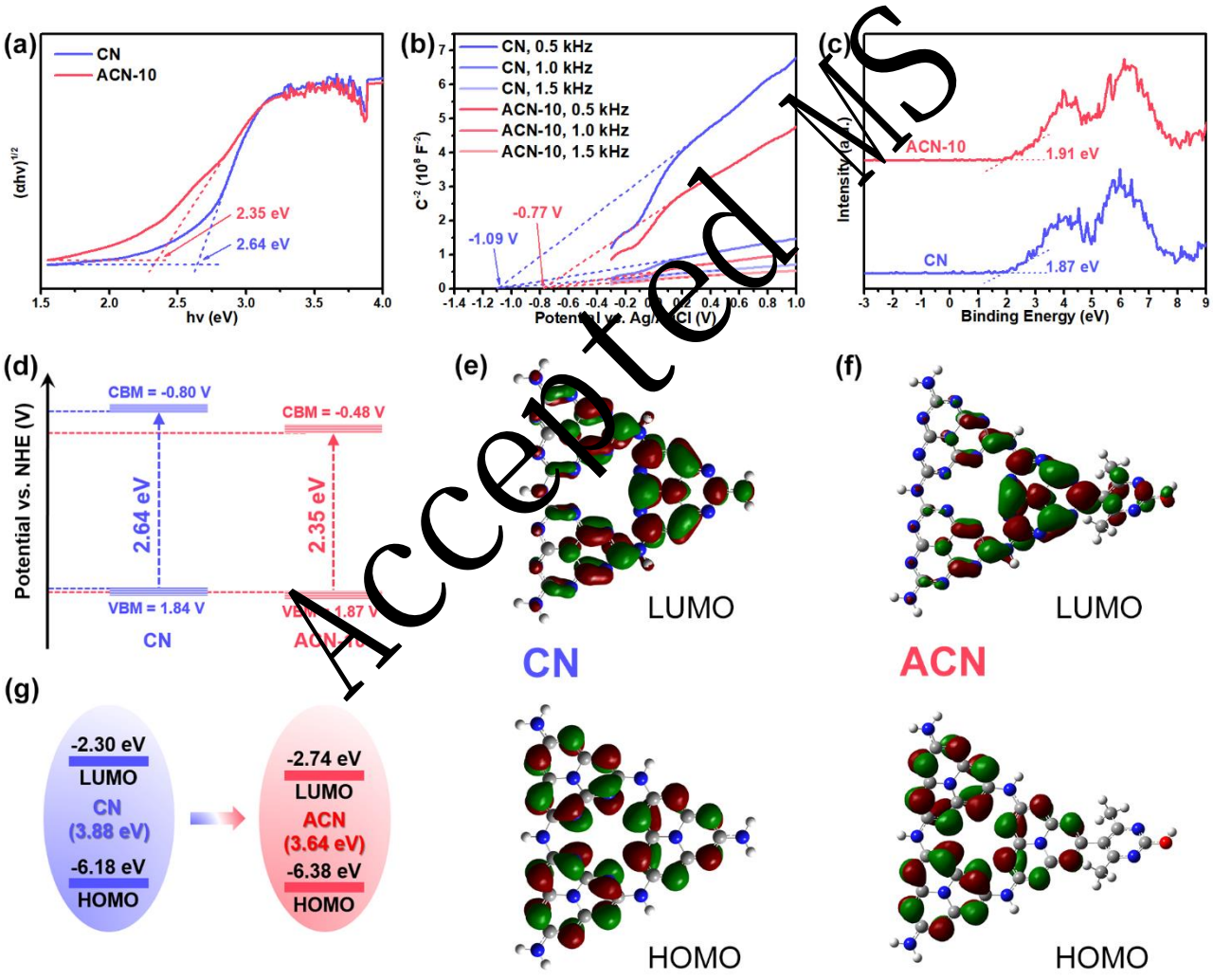

Fig. 4. (a) Tauc plots, (b) Mott-Schottky plots, (c) VB XPS spectra and (d) band structure diagrams for the CN and ACN-10; Optimized HOMO and LUMO energy levels of the (e) CN and (f) ACN; (g) DFT-calculated HOMO-LUMO band structures of the CN and ACN.

The band structures of CN and ACN-10 are analyzed by Tauc plots, Mott-Schottky plots and valence band (VB) XPS spectra. The Tauc plots derived from Fig. 3a are displayed in Fig. 4a. The band gaps obtained from the Tauc plots are 2.64 and 2.35 eV for CN and ACN-10, respectively. The narrowed band gap indicates that the ACN-10 possesses enhanced visible light harvesting ability as compared with CN. Fig. 4b shows the Mott-Schottky plots of CN and ACN-10 within frequencies ranging from 0.5 to 1.5 kHz. The obtained positive slopes imply that both CN and ACN-10 are n-type semiconductors. The flat band potentials of CN and ACN-10 are respectively estimated to be -1.09 V and -0.77 V vs Ag/AgCl [37]. Accordingly, their CB minimum (CBM) can be calculated from the following Eqs. (1) and (2) [53].

$$E_{\text{fb (vs NHE,pH=0)}} = E_{\text{fb (vs Ag/AgCl)}} + 0.059 \times \text{pH} + E_{(\text{AgCl})} \quad (1)$$

$$E_{\text{CBM (vs NHE)}} = E_{\text{fb (vs NHE,pH=0)}} - 0.3 \quad (2)$$

Where the pH of electrolyte is about 6.7 and $E_{(\text{AgCl})}$ is 0.197 V. Generally, the CBM of a n-type semiconductor is about 0.3 V more negative than E_{fb}. Thus, the CBM of CN and ACN-10 are determined to be -0.80 V and -0.48 V, respectively. And their VB maximum (VBM) are estimated to be 1.84 V and 1.87 V, which are in similar with the VB XPS spectra (Fig. 4c). The detailed band structure diagrams of CN and ACN-10 are depicted in Fig. 4d.

The DFT calculations are utilized to further elucidate the electronic structures and energy levels of CN and ACN. As shown in Fig. 4e, the HOMO of CN is mostly attributed to the combination of nitrogen p_z orbitals, and the LUMO is mainly derived from the C-N bond orbitals [42, 54]. The electrons on both HOMO and LUMO is located in the heptazine indicates that electrons and holes is located in the same heptazine units, which will lead to the rapid recombination of electrons and holes. However, the electrons of ACN are redistributed due to the electronegativity of HDMP. As exhibited in Fig. 4f, the HOMO of ACN is chiefly located in the heptazine units, whereas the LUMO of CAN

is mainly distributed in the HDMP moiety with slight part of in the heptazine near HDMP. This result demonstrates that electrons and holes are located in the HDMP and heptazine moiety, respectively, which will restrain their recombination and accelerate the spatial charge separation [55]. Moreover, the incorporation of HDMP into CN downshifts the energy levels of the HOMO and LUMO from -6.18 to -6.38 eV and -2.30 to -2.74 eV (Fig. 4g), respectively, resulting in a reduction of 0.24 eV in the band gap. The trend of change is in agreement with the results of Mott-Schottky plots and VB XPS spectra.

3.3. Photogenerated charge carrier dynamics

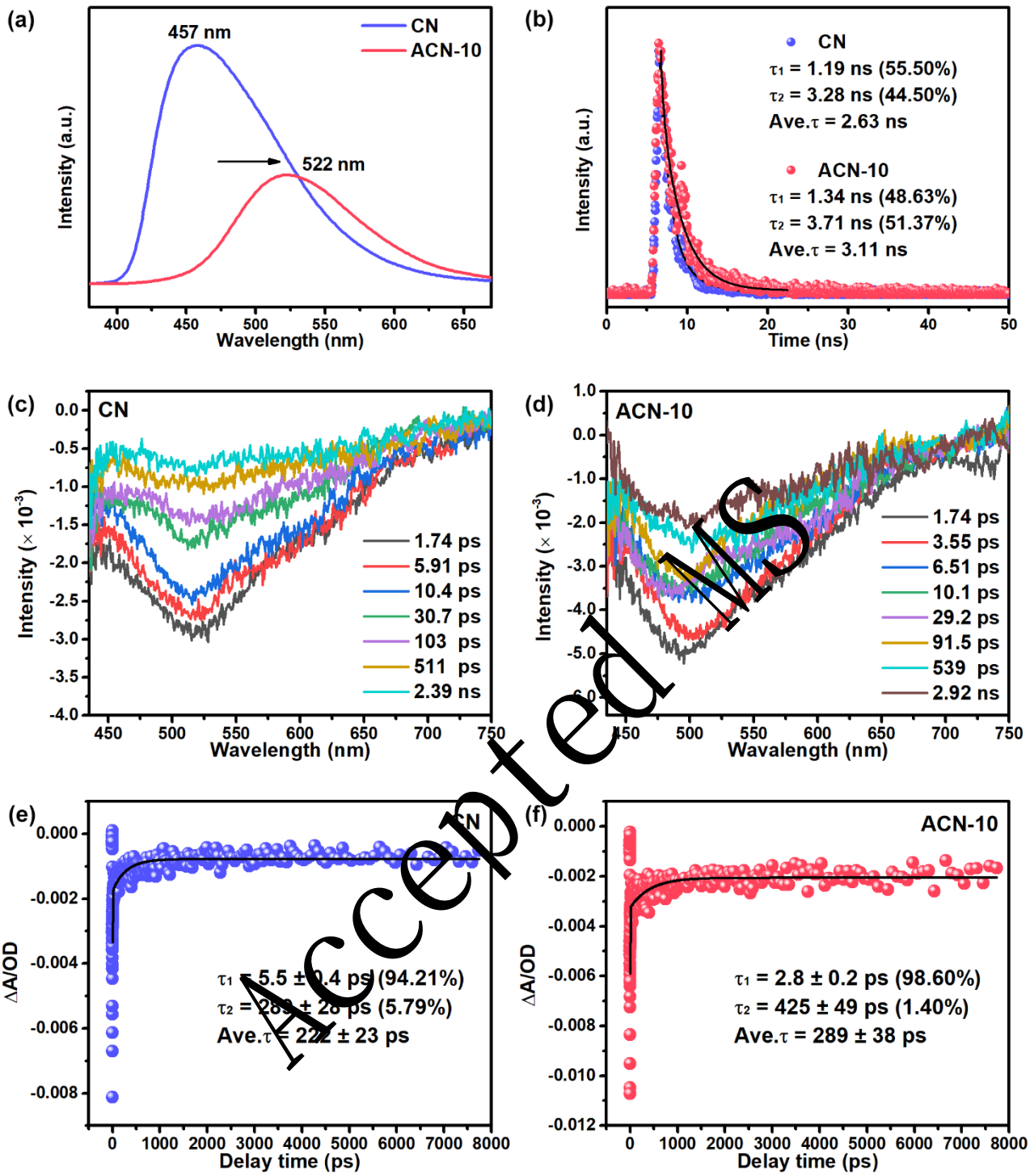

Fig. 5. (a) PL spectra and (b) TRPL spectra of the CN and ACN-10; fs-TA spectra and transient decay kinetics of the (c and e) CN and (d and f) ACN-10.

To clarify the separation and transfer behaviors of the photogenerated charge carriers, the PL spectra of CN and ACN-10 are measured under 350 nm excitation. As exhibited in Fig. 5a, compared with CN, the ACN-10 shows obviously reduced PL intensity, implying the inhibited radiative

recombination and the accelerated charge separation in ACN-10. Meanwhile, a red-shift of the PL peak from 457 nm for CN to 522 nm for ACN-10 can be observed, which results from the extension of π-conjugated system [47]. Furthermore, the TRPL spectra are recorded to quantitatively analyze the photogenerated charge carrier lifetimes of CN and ACN-10. As displayed in Fig. 5b, the fluorescence decay curves of them can be fitted by the following biexponential function (Eq. (3)) [56].

$$R(t) = B_1\exp(-t/\tau_1) + B_2\exp(-t/\tau_2) \quad (3)$$

Where B_1 and B_2 are the pre-exponential factor, and τ_1 and τ_2 are the short and long fluorescent lifetime, respectively. The average fluorescent lifetime (Ave.τ) can be calculated from the following Eq. (4).

$$\text{Ave.}\,\tau = \frac{B_1\tau_1^2+B_2\tau_2^2}{B_1\tau_1+B_2\tau_2} \quad (4)$$

The average fluorescent lifetime of CN and ACN-10 are 2.63 and 3.11 ns, respectively. The increased lifetime in ACN-10 signifies an enhanced transfer of photogenerated charges, thereby potentially improving the photocatalytic performance. To further explore the dynamics of photogenerated charge carriers, the fs-TA spectroscopy is utilized to detect transient absorption signals in real time. Fig. 5c and d display the evolution of the transient absorption spectra for CN and ACN-10, respectively. Under 400 nm laser excitation, both CN and ACN-10 exhibit a ground state bleaching signal in 450-700 nm region, which is originated from the stimulated emission [57, 58]. The signal intensity of ACN-10 is significantly enlarged compared with that of CN, implying that more photoinduced charge carriers are generated in ACN-10. The signals of CN and ACN-10 decay in the time range of 1.74 ps to 2.39 ns and 1.74 ps to 2.92 ns because of the recombination of photogenerated charge carriers [59, 60]. However, the decay lifetime in ACN-10 is much longer than that in CN, indicating the suppressed recombination of photogenerated electron-hole pairs in ACN-10 [61]. The transient decay kinetics of CN and ACN-10 are fitted by a biexponential function and the results are shown in the Fig. 5e and f, respectively. The average decay lifetime of CN is estimated to be (222 $\pm$ 23) ps. Compared to CN,

ACN-10 presents a longer average decay lifetime (289 ±38) ps, demonstrating that the incorporation of HDMP accelerates the intramolecular charge transfer and consequently inhibits charge recombination [62, 63]. On the basis of the PL, TRPL and fs-TA results, it can be concluded that the separation efficiency of photogenerated charge carriers over CN can be significantly enhanced by the incorporation of HDMP, which in turn ideally improves the photocatalytic performance.

3.4. Photocatalytic activities and mechanisms

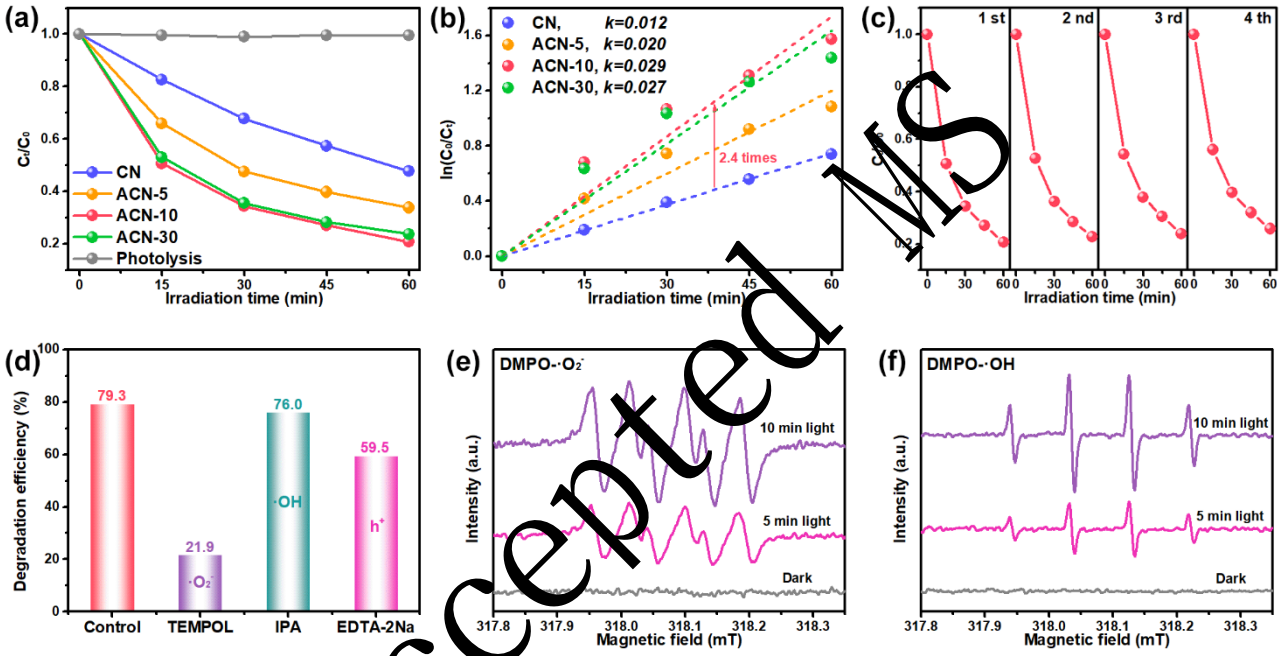

Fig. 6. (a) Photocatalytic degradation curves of OTC over different samples under visible light irradiation and (b) the corresponding pseudo-first-order kinetic curves; (c) Cycling runs for the photocatalytic degradation of OTC with ACN-10; (d) Photocatalytic degradation efficiency of OTC over the ACN-10 with different quenchers; ESR spectra of (e) DMPO-•O_2^- adduct and (f) DMPO-•OH adduct for the ACN-10.

The photocatalytic activity of the samples is assessed by the degradation of OTC under visible light irradiation. As exhibited in Fig. S5, the photocatalytic degradation of OTC is monitored by the variation on UV-vis absorption spectra of OTC solution. It is obvious that the intensity of characteristic absorption peak (353 nm) decreases with the time prolongs. Fig. 6a displays the change in OTC concentration (C_t/C_0) with irradiation time over the different samples under visible light

irradiation. The C_t represents the concentration of OTC after photocatalytic reaction for time *t*, and the C_0 refers to the initial concentration of OTC. The natural photolysis of OTC is negligible under visible light, indicating that the OTC is degraded by the photocatalysts. The degradation efficiencies for the ACN samples are all significantly higher than that of the CN sample. With an increasing volume of acetylacetone, the photocatalytic degradation activity of ACN presents an increasing trend. The highest photocatalytic degradation efficiency of OTC (79.3%) is achieved on ACN-10. Nevertheless, when the volume of acetylacetone exceeds 10 μL, the photocatalytic activity of ACN increases insignificantly because the over distorted structure may provide new recombination sites for electrons and holes. The apparent rate constant (*k*) for the degradation of OTC is obtained by the following Eq. (5).

$$k = \frac{\ln(C_0/C_t)}{t} \quad (5)$$

As shown in Fig. 6b, the plots of $\ln(C_0/C_t)$ versus *t* exhibits a linear relationship, indicating that the reaction is indeed pseudo-first-order. From the kinetic curves, the *k* value conforms the order: ACN-10 (0.029 min^{-1}) > ACN-30 (0.027 min^{-1}) > ACN-5 (0.020 min^{-1}) > CN (0.012 min^{-1}). The ACN-10 possesses the highest apparent rate constant of 0.029 min^{-1}, which is about 2.4 times than that of CN. The stability of the ACN-10 is evaluated through cyclic photocatalytic OTC degradation tests. In the cyclic experiments as displayed in Fig. 6c, the ACN-10 still exhibits high degradation efficiency without noticeable decrease. Furthermore, the XRD patterns, Raman spectra and ATR-FTIR spectra (Fig. S6) also verify that the crystal and the chemical structures of the ACN-10 keep almost unchanged after the photocatalytic reaction. In addition, the photocatalytic degradation activity of ACN-10 is higher than most of other CN-based photocatalysts reported previously (Table 1), indicating that the ACN may be a promising photocatalyst for photocatalytic degradation of organic pollutants.

Table 1

Comparison with other CN-based photocatalysts for degradation.

Photocatalysts	Pollutant concentration (mg L^{-1})	Dosage (g L^{-1})	Light source	k (min^{-1})	Ref.
β-Bi_2O_3@g-C_3N_4	TC (10)	0.50	250 W XL (λ > 420 nm)	0.031	[64]
Co_3O_4@CoO/g-C_3N_4	TC (10)	0.60	500 W XL (λ > 420 nm)	0.021	[65]
h-BN/g-C_3N_4	TC (10)	1.00	300 W XL (λ > 420 nm)	0.028	[66]
KMCN	TC (20)	1.00	300 W XL (λ > 420 nm)	0.028	[38]
CNF	TC (21)	0.50	300 W XL (λ > 420 nm)	0.014	[67]
BNQDs/UPCN	OTC (10)	1.00	300 W XL (λ > 420 nm)	0.031	[44]
OCN	OTC (20)	1.00	300 W XL (λ > 420 nm)	0.016	[68]
ACN	OTC (20)	0.30	300 W XL (λ > 420 nm)	0.029	This work

KMCN: potassium-doped porous ultrathin g-C_3N_4; CNF: carbon nitride foam; BNQDs/UPCN: boron nitride quantum dots decorated ultrathin porous g-C_3N_4; OCN: oxygen substituted g-C_3N_4; XL: Xenon lamp.

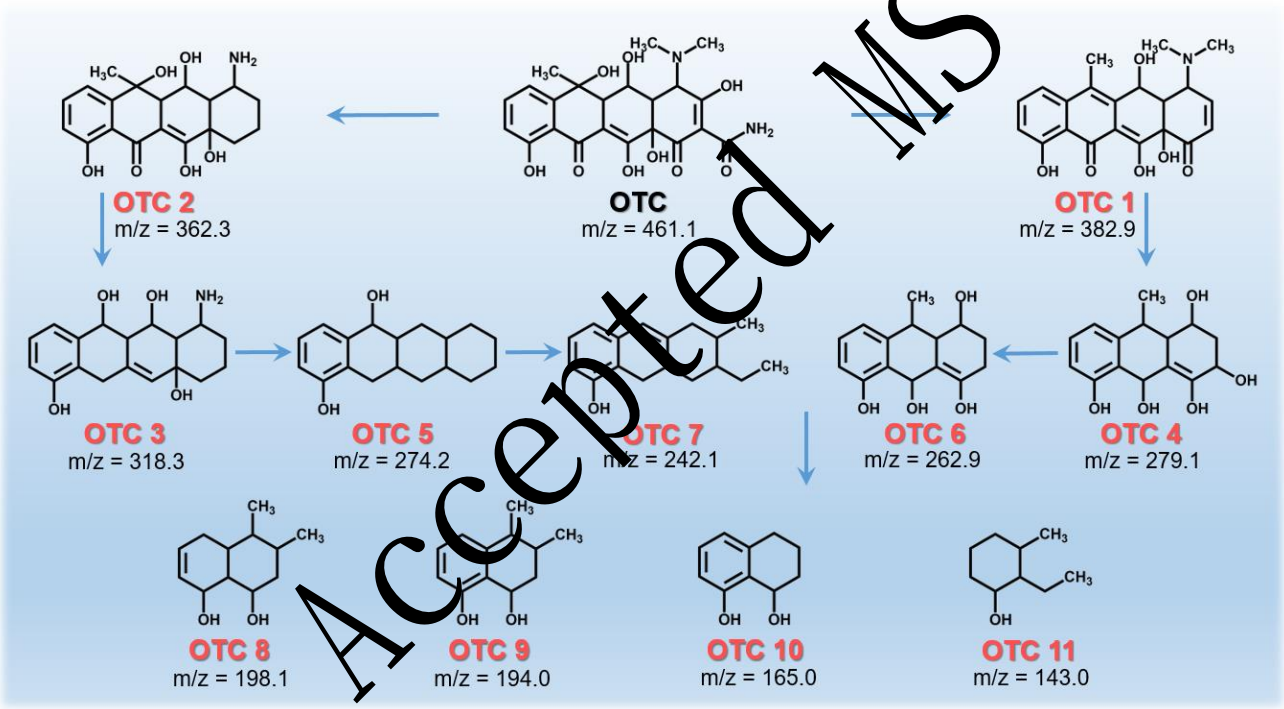

Scheme 1. The proposed photocatalytic degradation pathways of OTC over the ACN-10.

The preliminary degradation process of OTC over the ACN-10 is analyzed by LC-MS/MS technology. Fig. S7 and Table S2 show the MS spectra of the OTC solution after 60 min of degradation and the possible structures of intermediate products, respectively. According to the LC-MS/MS results and previous reports [69, 70], the possible photocatalytic degradation pathways of OTC are proposed and depicted in Scheme 1. Briefly, OTC (m/z = 461.1) is transformed to OTC 1

(m/z = 382.9) via the dehydration reaction, deamidation reaction and the loss of hydroxyl group. OTC 1 is then fragmented into OTC 4 (m/z = 279.1), which results to the formation of OTC 6 (m/z = 262.9) through the loss of hydroxyl group. Meanwhile, OTC can be also transformed to OTC 2 (m/z = 362.3) through the loss of *N*-methyl, carbonyl group and hydroxyl group as well as the deamidation reaction. With the loss of methyl, carbonyl group and hydroxyl group, the OTC 2 is decomposed to OTC 3 (m/z = 318.3). And the OTC 3 is transformed to OTC 5 (m/z = 274.2) through the loss of amino groups and oxidative dihydroxylation, then the OTC 5 is fragmented into OTC 7 (m/z = 242.1). Subsequently, these intermediates are oxidized to generate opening ring products including OTC 8 (m/z = 198.1), OTC 9 (m/z = 194.0), OTC 10 (m/z = 165.0) and OTC 11 (m/z = 143.0). Finally, these ring-opening products are oxidized into H_2O and CO_2. To evaluate the mineralization ability of ACN-10, the removal efficiency of TOC is analyzed. Fig. S8 shows that the removal efficiency of TOC in OTC aqueous solution is 15.4% with 60 min of visible light irradiation, further demonstrating the efficient photocatalytic activity of ACN-10 for OTC degradation.

To identify the main oxidative species generated in the ACN-10 under visible light irradiation for the degradation of OTC, the trapping experiments are conducted in the presence of quenchers. Herein, the TEMPOL, IPA and EDTA-2Na are utilized as the quenchers for $\bullet O_2^-$, •OH and h^+, respectively. As displayed in Fig. 6d, the degradation efficiency of OTC remarkably declines from 79.3% to 21.9% in the presence of TEMPOL. When EDTA-2Na is added into the photocatalytic system, the degradation efficiency of OTC slightly declines to 59.5%. Nevertheless, the addition of IPA has no obvious effect for the OTC degradation. Moreover, the generation of reactive oxygen species over the ACN-10 sample under visible light irradiation is monitored through a 5,5-dimethyl-1-pyrroline *N*-oxide (DMPO) spin-trapping ESR technique. As exhibited in Fig. 6e and f, no ESR signal can be detected in the dark. Upon visible light irradiation, two four-line ESR signals with an

intensity ratio of 1:1:1:1 and 1:2:2:1 are obviously observed, which are characteristic of DMPO-•O_2^- adduct and DMPO-•OH adduct, respectively. With the irradiation time prolongs, the intensity of the two adducts are all increase. These results demonstrate that the major reactive species for OTC degradation over the ACN-10 are •O_2^- and h^+, and that the •OH is involved but not primarily.

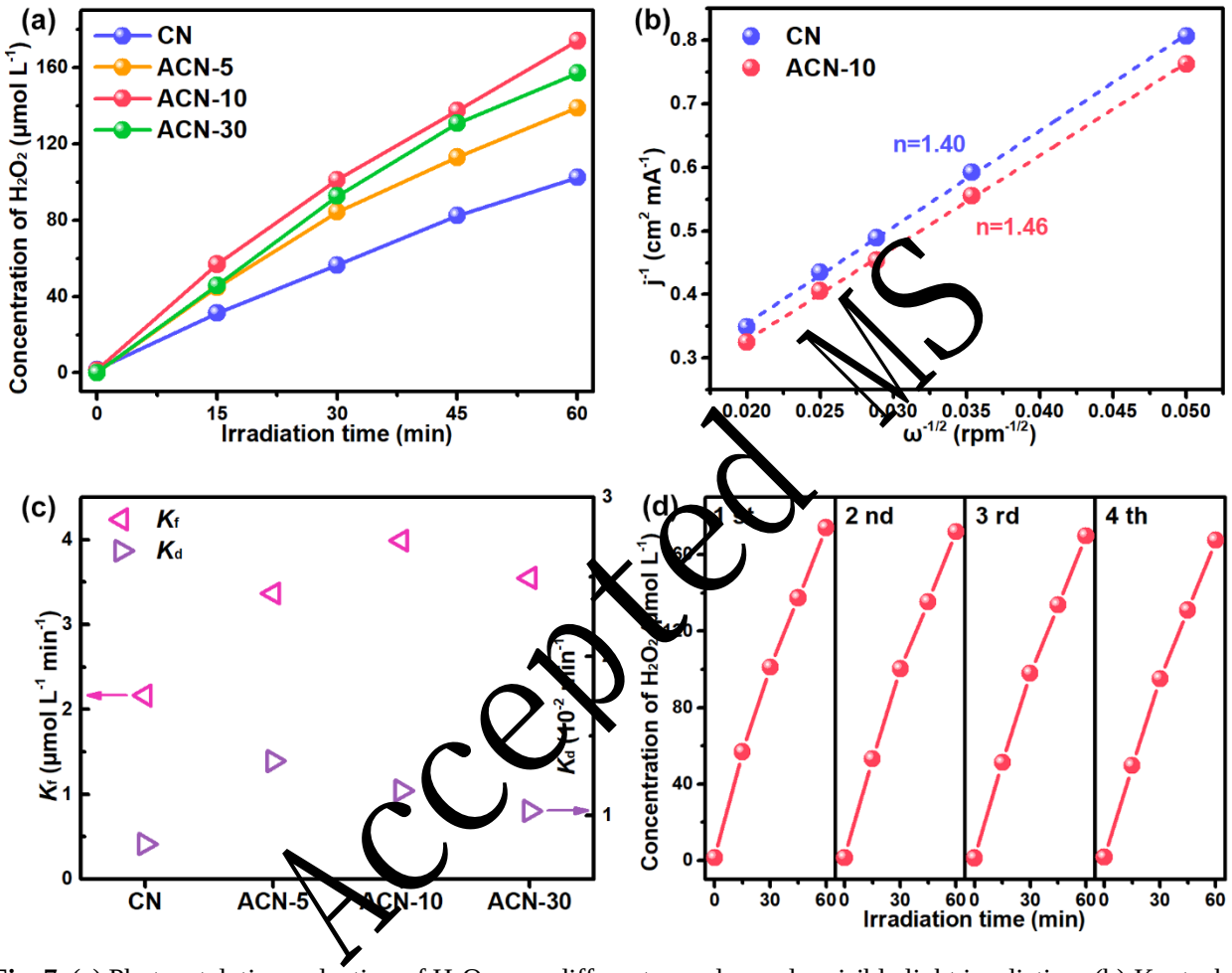

Fig. 7. (a) Photocatalytic production of H_2O_2 over different samples under visible light irradiation; (b) Koutecky-Levich plots of the data obtained at the constant electrode potential (-1.0 V vs. Ag/AgCl); (c) Formation rate constant (K_f) and decomposition rate constant (K_d) for photocatalytic H_2O_2 production; (d) Cycling runs for the photocatalytic H_2O_2 production over ACN-10.

The photocatalytic production of H_2O_2 is performed on an O_2-equilibrated IPA aqueous solution (10 vol%) under visible light irradiation. Fig. 7a displays the time-dependent H_2O_2 concentration over different samples. Obviously, the amount of H_2O_2 generated on ACN-10 is 174 μmol L^{-1}, which is

higher than that of CN (102 μmol L^{-1}), indicating that the incorporation of HDMP into CN enhances the yield of H_2O_2. However, the photocatalytic H_2O_2 production activity of ACN-30 is slightly inhibited because the over distorted structure may provide new recombination sites for charge carriers. Fig. S9 shows the UV-vis absorption spectra variations of ACN-10 during the H_2O_2 production process, in which the absorbance at 350 nm remarkably increases with the prolongation of irradiation time. Meanwhile, some controlled trials of H_2O_2 production is executed over ACN-10 (Fig. S10). In the absence of either photocatalyst or visible light irradiation, the H_2O_2 hardly can be detected, demonstrating that the H_2O_2 production process is accomplished by photocatalysis. Generally, the oxidation of H_2O through the photogenerated hole is also a possible route for H_2O_2 generation. Nevertheless, the H_2O_2 is scarcely generated when O_2 is replaced by Ar, and the generation of H_2O_2 is significantly inhibited in the absence of IPA. These results suggest that the H_2O_2 is generated from the electron reduction of O_2 rather than the oxidation of H_2O by the photogenerated hole [71, 72].

RDE measurements were performed to further clarify the numbers of electrons used for O_2 reduction. Fig. S11a and b exhibit the LSV curves of CN and ACN-10 collected on a RDE at different rotating speeds, respectively. The Koutecky-Levich plots of the data at -1.0 V vs. Ag/AgCl are displayed in Fig. 7b. The average numbers of electrons (n) involved in the overall reduction of O_2 can be estimated by the linear regression of the plots using the following Eqs. (6) and (7).

$$j^{-1} = j_k^{-1} + B^{-1}\omega^{-1/2} \quad (6)$$

$$B = 0.2nFv^{-1/6}CD^{2/3} \quad (7)$$

Where j is the measured current density, j_k is the kinetic current density, ω is the rotating speed (rpm), F is the Faraday constant (96485 C mol^{-1}), v is the kinetic viscosity of water (0.01 cm^2 s^{-1}), C is the bulk concentration of O_2 in water (1.26×10^{-3} mol cm^{-3}), and D is the diffusion coefficient of O_2 (2.7×10^{-5} cm^2 s^{-1}), respectively. Based on the intercept of the Koutecky-Levich plots, the j_k values of

CN and ACN-10 are evaluated to be 19.36 and 26.64 mA cm^{-2}, respectively, suggesting that O_2 is reduced more efficiently on ACN-10. According to the slope of the Koutecky-Levich plots, the *n* values of CN and ACN-10 are estimated to be 1.40 and 1.46, respectively. This result demonstrates that two-step single-electron O_2 reduction occurs on the CN and ACN-10, and the incorporation of HDMP into CN can promote the generation of electrons.

It is noted that the rate of H_2O_2 production is gradually decreased with the prolongation of irradiation time, indicating that the yield of H_2O_2 is restrained by its decomposition. In the photocatalytic production of H_2O_2, the formation and decomposition of H_2O_2 occur simultaneously because photogenerated charge carriers can decompose H_2O_2 [73]. To deeply understand the behavior of H_2O_2 production, the formation and decomposition of H_2O_2 are respectively assessed by assuming zero-order and first-order kinetics, as shown in the following Eq. (8) [13].

$$[H_2O_2] = \frac{K_f}{K_d}(1 - \exp(-K_d t)) \quad (8)$$

K_f and K_d are the rate constants for H_2O_2 formation (μmol L^{-1} min^{-1}) and decomposition (min^{-1}), respectively. The values of K_f and K_d are evaluated by fitting the data in Fig. 7a into Eq. (8) and the results are exhibited in Fig. 7c. After the incorporation of HDMP, the K_f value remarkably increases, achieving a maximum at ACN-10 which is about 1.8 times than CN (from 2.17 to 3.99 μmol L^{-1} min^{-1}), while the K_d value also increases but less significantly (from 0.82 × 10^{-2} to 1.16 × 10^{-2} min^{-1}). These results demonstrate that the incorporation of HDMP into CN can promote H_2O_2 formation and stabilize the formed H_2O_2 under visible light irradiation. Moreover, as shown in Fig. 7d, the cycle experiments for ACN-10 displays no apparent decrease in the photocatalytic production of H_2O_2 in four consecutive cycles, demonstrating that the photocatalyst is stable. In addition, the photocatalytic H_2O_2 production activities between the ACN-10 and other CN-based photocatalysts are compared in Table 2, indicating that the ACN may be a promising photocatalyst for photocatalytic H_2O_2

production.

Table 2

Comparison with other CN-based photocatalysts for H_2O_2 production.

Photocatalysts	Dosage (g L^{-1})	Reaction solution	Light source	H_2O_2 production activity (μmol g^{-1} h^{-1})	Ref.
g-C_3N_4/BDI	1.67	Water	Solar simulator (λ > 420 nm)	17.08	[35]
CN/rGO@BPQDs	1.00	Water	300 W XL (λ > 420 nm)	60.56	[17]
C, O doped g-C_3N_4	1.00	Water	300 W XL (λ > 420 nm)	32.00	[14]
Ag@U-g-C_3N_4-NS	1.00	Water	300 W XL (λ > 420 nm)	≈ 67.50	[13]
IO CN-Cv	1.00	5 vol% EA	300 W XL (λ > 420 nm)	162.87	[16]
Mesoporous g-C_3N_4	4.00	90 vol% EA	2 kW XL (λ > 420 nm)	≈ 183.50	[11]
DCN	0.83	20 vol% IPA	AM1.5 (λ > 420 nm)	96.80	[15]
Ti_3C_2/porous g-C_3N_4	1.00	10 vol% IPA	300 W XL (λ > 420 nm)	131.71	[31]
OCN	1.00	10 vol% IPA	300 W XL (λ > 420 nm)	1200.00	[37]
ACN	1.00	10 vol% IPA	300 W XL (λ > 420 nm)	174.00	This work

g-C_3N_4: graphitic carbon nitride; BDI: biphenyl diimide; rGO: reduced graphene oxide; BPQDs: black phosphorus quantum dots; U-g-C_3N_4-NS: ultrathin g-C_3N_4 nanosheets; IO CN-Cv: inverse opal structured CN with carbon vacancies; DCN: defective g-C_3N_4; OCN: oxygen-enriched carbon nitride polymer; EA: ethanol; IPA: isopropanol; XL: Xenon lamp.

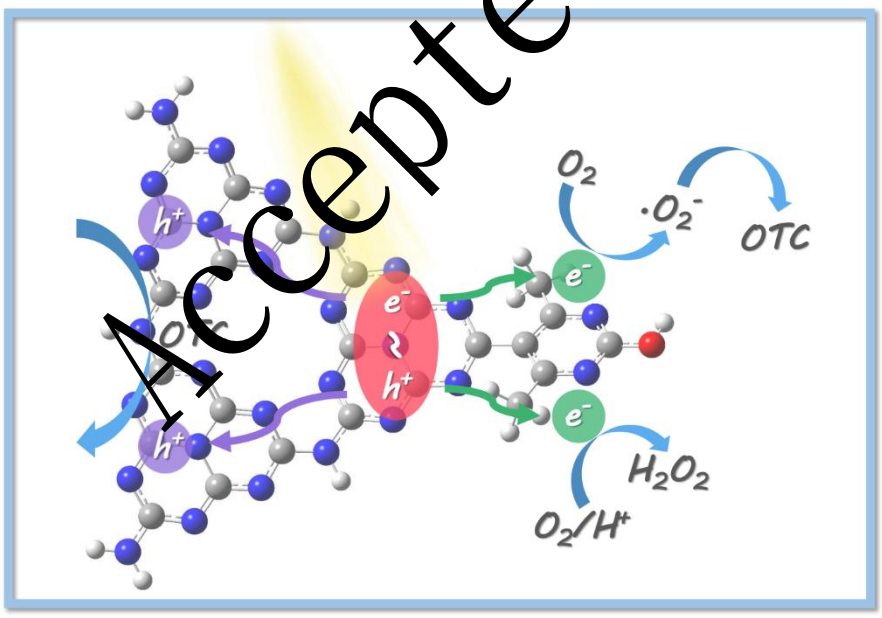

Scheme 2. The possible photocatalytic reaction mechanisms in ACN-10.

On the basis of the above results and discussion, the possible reaction mechanisms over the ACN-10 photocatalyst is described in Scheme 2. Under visible light irradiation, the photogenerated electron-hole pairs are produced on ACN-10 (Eq. (9)). Due to the uncoordinated polarity induced by

HDMP, the electron-hole pairs are rapidly separated. And the electrons and holes will eventually migrate to the HDMP and heptazine moiety, respectively. With respect to OTC degradation, the photogenerated electrons can react with adsorbed O_2 to form $\bullet O_2^-$ as the CBM of ACN-10 (-0.48 V vs NHE) is more negative than the redox potential of $O_2/\bullet O_2^-$ (-0.33 V vs NHE) (Eq. (10)). Meanwhile, some $\bullet O_2^-$ can further react with H^+ to form •OH (Eqs. (11) and (12)) [13, 26]. Subsequently, the photogenerated holes, $\bullet O_2^-$ and •OH will attack the OTC molecule, resulting in its degradation (Eq. (13)).

$$\text{ACN-10} + h\nu \rightarrow \text{ACN-10}\ (e^- + h^+) \quad (9)$$

$$e^- + O_2 \rightarrow \cdot O_2^- \quad (10)$$

$$\cdot O_2^- + e^- + 2H^+ \rightarrow H_2O_2 \quad (11)$$

$$H_2O_2 + e^- + 2H^+ \rightarrow H_2O + \cdot OH \quad (12)$$

$$(h^+, \cdot O_2^-, \cdot OH) + \text{OTC} \rightarrow CO_2 + H_2O + \text{products} \quad (13)$$

As for H_2O_2 production, H_2O_2 can be generated from the two-step single-electron O_2 reduction, as described by the following Eqs. (14-16).

$$CH_3CHOHCH_3 + 2h^+ \rightarrow CH_3COCH_3 + 2H^+ \quad (14)$$

$$e^- + O_2 \rightarrow \cdot O_2^- \quad (15)$$

$$\cdot O_2^- + e^- + 2H^+ \rightarrow H_2O_2 \quad (16)$$

Therefore, the ACN-10 photocatalyst present excellent photocatalytic activities in OTC degradation and H_2O_2 production, which is ascribed to the enhanced visible light absorption and boosted intramolecular charge separation.

4. Conclusion

In summary, a simple in situ keto-enol cyclization approach is developed to incorporate HDMP into the CN framework for modulating the electronic structure of CN. Benefitting from the

controllable electronic migration and boosted intramolecular charge separation, the ACN photocatalysts exhibit superior photocatalytic activities in OTC degradation and H_2O_2 production. At an optimized sample (ACN-10), 79.3% of OTC is degraded within 60 min of visible light irradiation, and the rate constant of the ACN-10 sample is nearly 2.4 times of that of pristine CN. And the photocatalytic H_2O_2 production rate of ACN-10 is 2.9 μmol L^{-1} min^{-1} under visible light irradiation, which is also higher than that of pristine CN (1.7 μmol L^{-1} min^{-1}). This work enables a deeper understanding of intramolecular charge separation in CN, and provides a generalizable approach to the refractory organic pollutants degradation and H_2O_2 production.

Acknowledgements

This study was financially supported by the Program for the National Natural Science Foundation of China (51521006, 51879101, 51579098, 51779090, 51709101, 51809090, 51278176, 51378190), the Three Gorges Follow-up Research Project (2017HXXY-05), the National Program for Support of Top-Notch Young Professionals of China (2014), the Program for Changjiang Scholars and Innovative Research Team in University (IRT-13R17), Hunan Provincial Science and Technology Plan Project (2018SK20410, 2017SK2243, 2016RS3026), Hunan Provincial Innovation Foundation For Postgraduate (CX20190233), the Natural Science Foundation of Hunan Province, China (Grant Nos. 2019JJ50077), and the Fundamental Research Funds for the Central Universities (531119200086, 531118010114, 531107050978, 541109060031).

References

[1] Y. Fu, L. Qin, D. Huang, G. Zeng, C. Lai, B. Li, J. He, H. Yi, M. Zhang, M. Cheng, Chitosan functionalized activated coke for Au nanoparticles anchoring: Green synthesis and catalytic activities in hydrogenation of nitrophenols and azo dyes, Appl. Catal. B: Environ., 255 (2019) 117740.

[2] C. Zhang, W. Wang, A. Duan, G. Zeng, D. Huang, C. Lai, X. Tan, M. Cheng, R. Wang, C. Zhou, Adsorption behavior of engineered carbons and carbon nanomaterials for metal endocrine disruptors: Experiments and theoretical calculation, Chemosphere, 222 (2019) 184-194.

[3] W. Xue, D. Huang, G. Zeng, J. Wan, C. Zhang, R. Xu, M. Cheng, R. Deng, Nanoscale zero-valent iron coated

with rhamnolipid as an effective stabilizer for immobilization of Cd and Pb in river sediments, J. Hazard. Mater., 341 (2018) 381-389.
[4] M. Jia, Z. Yang, H. Xu, P. Song, W. Xiong, J. Cao, Y. Zhang, Y. Xiang, J. Hu, C. Zhou, Integrating N and F co-doped TiO_2 nanotubes with ZIF-8 as photoelectrode for enhanced photo-electrocatalytic degradation of sulfamethazine, Chem. Eng. J., 388 (2020) 124388.
[5] S. Ye, G. Zeng, H. Wu, J. Liang, C. Zhang, J. Dai, W. Xiong, B. Song, S. Wu, J. Yu, The effects of activated biochar addition on remediation efficiency of co-composting with contaminated wetland soil, Resources, Conservation and Recycling, 140 (2019) 278-285.
[6] Z. Cai, A.D. Dwivedi, W. Lee, X. Zhao, W. Liu, M. Sillanpää, D. Zhao, C. Huang, J. Fu, Application of nanotechnologies for removing pharmaceutically active compounds from water: development and future trends, Environmental Science: Nano, 5 (2018) 27-47.
[7] H. Yi, M. Yan, D. Huang, G. Zeng, C. Lai, M. Li, X. Huo, L. Qin, S. Liu, X. Liu, Synergistic effect of artificial enzyme and 2D nano-structured Bi_2WO_6 for eco-friendly and efficient biomimetic photocatalysis, Appl. Catal. B: Environ., 250 (2019) 52-62.
[8] S. Tian, C. Zhang, D. Huang, R. Wang, G. Zeng, M. Yan, W. Xiong, C. Zhou, M. Cheng, W. Xue, Recent progress in sustainable technologies for adsorptive and reactive removal of sulfonamides, Chem. Eng. J., (2019) 123423.
[9] Y. Liu, M. Cheng, Z. Liu, G. Zeng, H. Zhong, M. Chen, C. Zhou, W. Xiong, B. Shao, B. Song, Heterogeneous Fenton-like catalyst for treatment of rhamnolipid-solubilized hexadecane wastewater, Chemosphere, 236 (2019) 124387.
[10] Y. Kawase, Y. Isaka, Y. Kuwahara, K. Mori, H. Yamashita, Ti cluster-alkylated hydrophobic MOFs for photocatalytic production of hydrogen peroxide in two-phase systems, Chem. Commun., 55 (2019) 6743-6746.
[11] Y. Shiraishi, Y. Kofuji, H. Sakamoto, S. Tanaka, S. Ichikawa, T. Hirai, Effects of surface defects on photocatalytic H_2O_2 production by mesoporous graphitic carbon nitride under visible light irradiation, ACS Catal., 5 (2015) 3058-3066.
[12] L. Qin, Z. Zeng, G. Zeng, C. Lai, A. Duan, R. Xiao, D. Huang, Y. Fu, H. Yi, B. Li, Cooperative catalytic performance of bimetallic Ni-Au nanocatalyst for highly efficient hydrogenation of nitroaromatics and corresponding mechanism insight, Appl. Catal. B: Environ., 259 (2019) 118035.
[13] J. Cai, J. Huang, S. Wang, J. Iocozzia, Z. Sun, J. Sun, Y. Yang, Y. Lai, Z. Lin, Crafting mussel-inspired metal nanoparticle-decorated ultrathin graphitic carbon nitride for the degradation of chemical pollutants and production of chemical resources, Adv. Mater., 31 (2019) 1806314.
[14] S. Samanta, R. Yadav, A. Kumar, A.K. Sinha, R. Srivastava, Surface modified C, O co-doped polymeric g-C_3N_4 as an efficient photocatalyst for visible light assisted CO_2 reduction and H_2O_2 production, Appl. Catal. B: Environ., 259 (2019) 118054.
[15] L. Shi, L. Yang, W. Zhou, Y. Liu, L. Yin, X. Hai, H. Song, J. Ye, Photoassisted construction of holey defective g-C_3N_4 photocatalysts for efficient visible-light-driven H_2O_2 production, Small, 14 (2018) 1703142.
[16] J. Lei, B. Chen, W. Lv, L. Zhou, L. Wang, Y. Liu, J. Zhang, Robust photocatalytic H_2O_2 production over inverse opal g-C_3N_4 with carbon vacancy under visible light, ACS Sustain. Chem. Eng., 7 (2019) 16467-16473.
[17] J. Xiong, X. Li, J. Huang, X. Gao, Z. Chen, J. Liu, H. Li, B. Kang, W. Yao, Y. Zhu, CN/rGO@ BPQDs high-low junctions with stretching spatial charge separation ability for photocatalytic degradation and H_2O_2 production, Appl. Catal. B: Environ., (2020) 118602.
[18] H. Wang, Z. Zeng, P. Xu, L. Li, W. Tang, Recent progress in covalent organic framework thin films: fabrications, applications and perspectives, Chem. Soc. Rev., 48 (2019) 488-516.
[19] Y. Yang, C. Zhang, C. Lai, G. Zeng, D. Huang, M. Cheng, J. Wang, F. Chen, C. Zhou, W. Xiong, BiOX (X= Cl, Br, I) photocatalytic nanomaterials: applications for fuels and environmental management, Adv. Colloid Interface Sci., 254 (2018) 76-93.

[20] W. Xue, Z. Peng, D. Huang, G. Zeng, X. Wen, R. Deng, Y. Yang, X. Yan, In situ synthesis of visible-light-driven Z-scheme AgI/Bi_2WO_6 heterojunction photocatalysts with enhanced photocatalytic activity, Ceram. Int., 45 (2019) 6340-6349.
[21] X. Li, P. Xu, M. Chen, G. Zeng, D. Wang, F. Chen, W. Tang, C. Chen, C. Zhang, X. Tan, Application of silver phosphate-based photocatalysts: Barriers and solutions, Chem. Eng. J., 366 (2019) 339-357.
[22] H. Yi, M. Jiang, D. Huang, G. Zeng, C. Lai, L. Qin, C. Zhou, B. Li, X. Liu, M. Cheng, Advanced photocatalytic Fenton-like process over biomimetic hemin-Bi_2WO_6 with enhanced pH, J. Taiwan Inst. Chem. Eng., 93 (2018) 184-192.
[23] D. He, C. Zhang, G. Zeng, Y. Yang, D. Huang, L. Wang, H. Wang, A multifunctional platform by controlling of carbon nitride in the core-shell structure: from design to construction, and catalysis applications, Appl. Catal. B: Environ., (2019) 117957.
[24] Q. Hao, G. Jia, W. Wei, A. Vinu, Y. Wang, H. Arandiyan, B. Ni, Graphitic carbon nitride with different dimensionalities for energy and environmental applications, Nano Res., 13 (2020) 18-37.
[25] C. Choi, L. Lin, S. Gim, S. Lee, H. Kim, X. Wang, W. Choi, Polymeric carbon nitride with localized aluminum coordination sites as a durable and efficient photocatalyst for visible light utilization, ACS Catal., 8 (2018) 4241-4256.
[26] W. Liu, Y. Li, F. Liu, W. Jiang, D. Zhang, J. Liang, Visible-light-driven photocatalytic degradation of diclofenac by carbon quantum dots modified porous g-C_3N_4: Mechanisms, degradation pathway and DFT calculation, Water Res., 151 (2019) 8-19.
[27] X. Wang, K. Maeda, A. Thomas, K. Takanabe, G. Xin, J.M. Carlsson, K. Domen, M. Antonietti, A metal-free polymeric photocatalyst for hydrogen production from water under visible light, Nat. Mater., 8 (2009) 76-80.
[28] Y. Shiraishi, S. Kanazawa, Y. Sugano, D. Tsukamoto, H. Sakamoto, S. Ichikawa, T. Hirai, Highly selective production of hydrogen peroxide on graphitic carbon nitride (g-C_3N_4) photocatalyst activated by visible light, ACS Catal., 4 (2014) 774-780.
[29] B. Song, Z. Zeng, G. Zeng, J. Gong, R. Xiao, S. Ye, M. Chen, C. Lai, P. Xu, X. Tang, Powerful combination of g-C_3N_4 and LDHs for enhanced photocatalytic performance: A review of strategy, synthesis, and applications, Adv. Colloid Interface Sci., (2019) 101999.
[30] Q. Hao, Y. Huang, D. Chen, Y. Liu, W. Wei, B. Ni, Accelerated separation of photogenerated charge carriers and enhanced photocatalytic performance of g-C_3N_4 by Bi_2S_3 nanoparticles, Chin. J. Catal., 41 (2020) 249-258.
[31] Y. Yang, Z. Zeng, G. Zeng, D. Huang, R. Xiao, C. Zhang, C. Zhou, W. Xiong, W. Wang, M. Cheng, Ti_3C_2 Mxene/porous g-C_3N_4 interfacial Schottky junction for boosting spatial charge separation in photocatalytic H_2O_2 production, Appl. Catal. B: Environ., 258 (2019) 117956.
[32] H. Ji, P. Du, D. Zhao, S. Li, F. Sun, E.C. Duin, W. Liu, 2D/1D graphitic carbon nitride/titanate nanotubes heterostructure for efficient photocatalysis of sulfamethazine under solar light: Catalytic “hot spots” at the rutile-anatase-titanate interfaces, Appl. Catal. B: Environ., 263 (2020) 118357.
[33] Z. Zhou, Y. Zhang, Y. Shen, S. Liu, Y. Zhang, Molecular engineering of polymeric carbon nitride: advancing applications from photocatalysis to biosensing and more, Chem. Soc. Rev., 47 (2018) 2298-2321.
[34] C. Zhou, G. Zeng, D. Huang, Y. Luo, M. Cheng, Y. Liu, W. Xiong, Y. Yang, B. Song, W. Wang, Distorted polymeric carbon nitride via carriers transfer bridges with superior photocatalytic activity for organic pollutants oxidation and hydrogen production under visible light, J. Hazard. Mater., 386 (2020) 121947.
[35] Y. Kofuji, S. Ohkita, Y. Shiraishi, H. Sakamoto, S. Tanaka, S. Ichikawa, T. Hirai, Graphitic carbon nitride doped with biphenyl diimide: efficient photocatalyst for hydrogen peroxide production from water and molecular oxygen by sunlight, ACS Catal., 6 (2016) 7021-7029.
[36] H.-i. Kim, Y. Choi, S. Hu, W. Choi, J.-H. Kim, Photocatalytic hydrogen peroxide production by anthraquinone-augmented polymeric carbon nitride, Appl. Catal. B: Environ., 229 (2018) 121-129.

[37] Z. Wei, M. Liu, Z. Zhang, W. Yao, H. Tan, Y. Zhu, Efficient visible-light-driven selective oxygen reduction to hydrogen peroxide by oxygen-enriched graphitic carbon nitride polymers, Energy Environ. Sci., 11 (2018) 2581-2589.
[38] W. Wang, P. Xu, M. Chen, G. Zeng, C. Zhang, C. Zhou, Y. Yang, D. Huang, C. Lai, M. Cheng, Alkali metal assisted synthesis of graphite carbon nitride with tunable band-gap for enhanced visible-light-driven photocatalytic performance, ACS Sustain. Chem. Eng., 6 (2018) 15503-15516.
[39] Y. Wang, F. Silveri, M. Bayazit, Q. Ruan, Y. Li, J. Xie, C.R. Catlow, J. Tang, Bandgap engineering of organic semiconductors for highly efficient photocatalytic water splitting, Adv. Energy Mater., 8 (2018) 1801084.
[40] C. Zhou, P. Xu, C. Lai, C. Zhang, G. Zeng, D. Huang, M. Cheng, L. Hu, W. Xiong, X. Wen, Rational design of graphic carbon nitride copolymers by molecular doping for visible-light-driven degradation of aqueous sulfamethazine and hydrogen evolution, Chem. Eng. J., 359 (2019) 186-196.
[41] H. Song, G. Liu, J. Zhang, J. Wu, Pyrolysis characteristics and kinetics of low rank coals by TG-FTIR method, Fuel Process. Technol., 156 (2017) 454-460.
[42] Z. Li, S. Zhou, Q. Yang, Z. Zhang, X. Fang, Insight into the enhanced hydrogen evolution activity of 2,4-diaminopyrimidine-doped graphitic carbon nitride photocatalysts, J. Phys. Chem. C, 123 (2019) 2228-2237.
[43] D. Adsmond, A. Sinha, U. Khandavilli, A. Maguire, S. Lawrence, Design and synthesis of ternary cocrystals using carboxyphenols and two complementary acceptor compounds, Cryst. Growth Des., 16 (2016) 59-69.
[44] Y. Yang, C. Zhang, D. Huang, G. Zeng, J. Huang, C. Lai, C. Zhou, W. Wang, H. Guo, W. Xue, Boron nitride quantum dots decorated ultrathin porous g-C_3N_4: intensified exciton dissociation and charge transfer for promoting visible-light-driven molecular oxygen activation, Appl. Catal. B: Environ., 245 (2019) 87-99.
[45] W. Wang, Z. Zeng, G. Zeng, C. Zhang, R. Xiao, C. Zhou, W. Xiong, Y. Yang, L. Lei, Y. Liu, D. Huang, M. Cheng, Y. Yang, Y. Fu, H. Luo, Y. Zhou, Sulfur doped carbon quantum dots loaded hollow tubular g-C_3N_4 as novel photocatalyst for destruction of *Escherichia coli* and tetracycline degradation under visible light, Chem. Eng. J., 378 (2019) 122132.
[46] N. Meng, W. Zhou, Y. Yu, Y. Liu, B. Zhang, Superficial hydroxyl and amino groups synergistically active polymeric carbon nitride for CO_2 electroreduction, ACS Catal., 9 (2019) 10983-10989.
[47] J. Li, D. Wu, J. Iocozzia, H. Du, X. Liu, Y. Yuan, W. Zhou, Z. Li, Z. Xue, Z. Lin, Achieving efficient incorporation of π-electrons into graphitic carbon nitride for markedly improved hydrogen generation, Angew. Chem. Int. Ed., 131 (2019) 2007-2011.
[48] Z. Sun, Y. Jiang, L. Zeng, L. Huang, Intramolecular charge transfer and extended conjugate effects in donor-π-acceptor-type mesoporous carbon nitride for photocatalytic hydrogen evolution, ChemSusChem, 12 (2019) 1325-1333.
[49] Y. Gao, Y. Zhu, L. Lyu, Q. Zeng, C. Hu, Electronic structure modulation of graphitic carbon nitride by oxygen doping for enhanced catalytic degradation of organic pollutants through peroxymonosulfate activation, Environ. Sci. Technol., 52 (2018) 14371-14380.
[50] Z. Sun, Y. Jiang, L. Zeng, X. Zhang, S. Hu, L. Huang, Controllable local electronic migration induced charge separation and red-shift emission in carbon nitride for enhanced photocatalysis and potential phototherapy, Chem. Commun., 55 (2019) 6002-6005.
[51] H. Guo, H. Niu, C. Liang, C. Niu, D. Huang, L. Zhang, N. Tang, Y. Yang, C. Feng, G. Zeng, Insight into the energy band alignment of magnetically separable $Ag_2O/ZnFe_2O_4$ p-n heterostructure with rapid charge transfer assisted visible light photocatalysis, J. Catal., 370 (2019) 289-303.
[52] Y. Lin, X. Wu, Y. Han, C. Yang, Y. Ma, C. Du, Q. Teng, H. Liu, Y. Zhong, Spatial separation of photogenerated carriers and enhanced photocatalytic performance on Ag_3PO_4 catalysts via coupling with PPy and MWCNTs, Appl. Catal. B: Environ., 258 (2019) 117969.
[53] W. Ong, L. Putri, Y. Tan, L. Tan, N. Li, Y. Ng, X. Wen, S. Chai, Unravelling charge carrier dynamics in protonated

g-C_3N_4 interfaced with carbon nanodots as co-catalysts toward enhanced photocatalytic CO_2 reduction: a combined experimental and first-principles DFT study, Nano Res., 10 (2017) 1673-1696.
[54] K. Li, W. Zhang, Creating graphitic carbon nitride based donor-π-acceptor-π-donor structured catalysts for highly photocatalytic hydrogen evolution, Small, 14 (2018) e1703599.
[55] H. Gao, Y. Guo, Z. Yu, M. Zhao, Y. Hou, Z. Zhu, S. Yan, Q. Liu, Z. Zou, Incorporating *para*-phenylene as an electron-donating group into graphitic carbon nitride for efficient charge separation, ChemSusChem, 12 (2019) 4285-4292.
[56] Y. Yu, W. Yan, X. Wang, P. Li, W. Gao, H. Zou, S. Wu, K. Ding, Surface engineering for extremely enhanced charge separation and photocatalytic hydrogen evolution on g-C_3N_4, Adv. Mater., 30 (2018) 1705060.
[57] M. Rahman, C. Mullins, Understanding charge transport in carbon nitride for enhanced photocatalytic solar fuel production, Accounts Chem. Res., 52 (2018) 248-257.
[58] C. Zhao, Z. Chen, J. Xu, Q. Liu, H. Xu, H. Tang, G. Li, Y. Jiang, F. Qu, Z. Lin, Probing supramolecular assembly and charge carrier dynamics toward enhanced photocatalytic hydrogen evolution in 2D graphitic carbon nitride nanosheets, Appl. Catal. B: Environ., 256 (2019) 117867.
[59] K. Corp, C. Schlenker, Ultrafast spectroscopy reveals electron-transfer cascade that improves hydrogen evolution with carbon nitride photocatalysts, JACS, 139 (2017) 7904-7912.
[60] W. Lei, Y. Mi, R. Feng, P. Liu, S. Hu, J. Yu, X. Liu, J. Rodriguez, J. Wang, L. Zheng, Hybrid 0D-2D black phosphorus quantum dots-graphitic carbon nitride nanosheets for efficient hydrogen evolution, Nano Energy, 50 (2018) 552-561.
[61] M. Zhu, S. Kim, L. Mao, M. Fujitsuka, J. Zhang, X. Wang, T. Majima, Metal-free photocatalyst for H_2 evolution in visible to near-infrared region: black phosphorus/graphitic carbon nitride, JACS, 139 (2017) 13234-13242.
[62] O. Elbanna, P. Zhang, M. Fujitsuka, T. Majima, Facile preparation of nitrogen and fluorine codoped TiO_2 mesocrystal with visible light photocatalytic activity, Appl. Catal. B: Environ., 192 (2016) 80-87.
[63] J. Xu, M. Fujitsuka, S. Kim, Z. Wang, T. Majima, Unprecedented effect of CO_2 calcination atmosphere on photocatalytic H_2 production activity from water using g-C_3N_4 synthesized from triazole polymerization, Appl. Catal. B: Environ., 241 (2019) 141-148.
[64] Y. Hong, C. Li, B. Yin, D. Li, Z. Zhang, B. Mao, W. Fan, W. Gu, W. Shi, Promoting visible-light-induced photocatalytic degradation of tetracycline by an efficient and stable beta-Bi_2O_3@g-C_3N_4 core/shell nanocomposite, Chem. Eng. J., 338 (2018) 137-146.
[65] J. Zheng, L. Zhang, Designing 3D magnetic peony flower-like cobalt oxides/g-C_3N_4 dual Z-scheme photocatalyst for remarkably enhanced sunlight driven photocatalytic redox activity, Chem. Eng. J., 369 (2019) 947-956.
[66] L. Jiang, X. Yuan, G. Zeng, Z. Wu, J. Liang, X. Chen, L. Leng, H. Wang, H. Wang, Metal-free efficient photocatalyst for stable visible-light photocatalytic degradation of refractory pollutant, Appl. Catal. B: Environ., 221 (2018) 715-725.
[67] H. Wang, Y. Wu, M. Feng, W. Tu, T. Xiao, T. Xiong, H. Ang, X. Yuan, J.W. Chew, Visible-light-driven removal of tetracycline antibiotics and reclamation of hydrogen energy from natural water matrices and wastewater by polymeric carbon nitride foam, Water Res., 144 (2018) 215-225.
[68] H. Guo, C. Niu, C. Feng, C. Liang, L. Zhang, X. Wen, Y. Yang, H. Liu, L. Li, L. Lin, Steering exciton dissociation and charge migration in green synthetic oxygen-substituted ultrathin porous graphitic carbon nitride for boosted photocatalytic reactive oxygen species generation, Chem. Eng. J., 385 (2020) 123919.
[69] J. Cao, S. Sun, X. Li, Z. Yang, W. Xiong, Y. Wu, M. Jia, Y. Zhou, C. Zhou, Y. Zhang, Efficient charge transfer in aluminum-cobalt layered double hydroxide derived from Co-ZIF for enhanced catalytic degradation of tetracycline through peroxymonosulfate activation, Chem. Eng. J., 382 (2020) 122802.
[70] Y. Yang, Z. Zeng, C. Zhang, D. Huang, G. Zeng, R. Xiao, C. Lai, C. Zhou, H. Guo, W. Xue, Construction of iodine

vacancy-rich BiOI/Ag@AgI Z-scheme heterojunction photocatalysts for visible-light-driven tetracycline degradation: transformation pathways and mechanism insight, Chem. Eng. J., 349 (2018) 808-821.
[71] G. Moon, M. Fujitsuka, S. Kim, T. Majima, X. Wang, W. Choi, Eco-friendly photochemical production of H_2O_2 through O_2 reduction over carbon nitride frameworks incorporated with multiple heteroelements, ACS Catal., 7 (2017) 2886-2895.
[72] Y. Zheng, Z. Yu, H. Ou, A. Asiri, Y. Chen, X. Wang, Black phosphorus and polymeric carbon nitride heterostructure for photoinduced molecular oxygen activation, Adv. Funct. Mater., 28 (2018) 1705407.
[73] Y. Isaka, Y. Kondo, Y. Kawase, Y. Kuwahara, K. Mori, H. Yamashita, Photocatalytic production of hydrogen peroxide through selective two-electron reduction of dioxygen utilizing amine-functionalized MIL-125 deposited with nickel oxide nanoparticles, Chem. Commun., 54 (2018) 9270-9273.